

Thermoelectric Properties of Anisotropic Systems

W. E. Bies, R. J. Radtke, and H. Ehrenreich

*Physics Department and the Division of Engineering and Applied Sciences,
Harvard University, Cambridge, Massachusetts 02138*

The effective transport coefficients and figure of merit ZT for anisotropic systems are derived from a macroscopic formalism. The full tensorial structure of the transport coefficients and the effect of the sample boundaries are included. Induced transverse fields develop which can be larger than the applied fields and which reduce the effective transport coefficients. A microscopic model relevant for multi-valleyed materials is introduced which utilizes the effective-mass and relaxation-time approximations. The thermopower and Lorentz number are independent of the tensorial structure of the transport coefficients in this case and are therefore isotropic. ZT is also isotropic for vanishing lattice thermal conductivity κ_ℓ . For non-vanishing but sufficiently isotropic κ_ℓ , ZT is maximal along the direction of highest electrical conductivity σ . Numerical calculations suggest that maximal ZT generally occurs along the principal direction with the largest σ/κ_ℓ . An explicit bound on ZT is derived. Several results for specific systems are obtained: (1) Bulk n-type Bi_2Te_3 exhibits easily observable induced transverse fields and anisotropic ZT s. (2) Increased anisotropy in $\text{HgTe}/\text{Hg}_{1-x}\text{Cd}_x\text{Te}$ superlattices (SLs) is associated with larger induced fields. (3) The valley degeneracy is split and the bulk masses modified in isolated Bi_2Te_3 quantum wells, resulting in optimal ZT s for wells grown along the trigonal direction. (4) Non-parabolic dispersion in SLs has little effect on the thermopower at the carrier concentrations which maximize ZT .

PACS numbers: 72.20.Pa, 72.10.Bg, 73.20.Dx

I. INTRODUCTION

In the search to find systems with large thermoelectric figures of merit ZT , the emphasis has been more on new materials than on materials structures or crystallographic anisotropy. Typical of new structures are superlattices, quantum wells¹⁻⁸ and quantum wires.^{9,10} It has been generally assumed that the direction of highest conductivity in an anisotropic material yields optimal thermoelectric properties. The correctness of this assumption is not obvious, since directions may exist along which the lattice thermal conductivity is abnormally low and the thermopower is high enough to result in large ZT even though the electrical conductivity is less than maximum.

This paper develops a more general transport theory of thermoelectricity in anisotropic systems. The “highest conductivity” assumption is found to be correct for materials having simple band structures typically of the parabolic variety and essentially isotropic lattice thermal conductivities. However, the formalism developed here suggests more generally that the optimal orientation corresponds to the principal direction along which the ratio of the electronic to lattice thermal conductivity σ/κ_ℓ is maximum. There are also several surprising results. These include the formation of possibly large induced transverse electric fields and temperature gradients, the fact that ZT is strictly isotropic in anisotropic systems having parabolic bands if the lattice thermal conductivity is neglected, and that a nearly isotropic thermopower and Lorentz number results under these conditions even if the bands are extremely anisotropic and non-parabolic.

The macroscopic formalism, based on the tensorial form of the usual phenomenological transport equations, is presented in Sec. II. The effects of sample boundaries are included by requiring that the transverse electric and heat currents vanish at the transverse surfaces. Anisotropic and isotropic systems are shown to differ both qualitatively, through the presence of induced transverse fields, and quantitatively, through the magnitude of the transport coefficients.

More detailed statements concerning optimal orientations require use of a microscopic model. Section III introduces a model commonly used to study transport in semiconductors having multi-valley, anisotropic band structures. The transport properties follow from the linearized Boltzmann equation in the effective-mass and relaxation-time approximations. Intervalley scattering is neglected. The thermopower and Lorentz number somewhat surprisingly turn out to be isotropic. The same is true for ZT when the lattice thermal conductivity κ_ℓ is neglected. Sec. IIIB shows that similar results hold for two- and one-dimensional systems. The realistic case corresponding to finite κ_ℓ is considered in Sec. IIIC. If κ_ℓ is sufficiently isotropic, the maximal ZT is shown to occur for samples cut along the direction of highest electrical conductivity. This rather unsurprising result, however, may be modified if the anisotropy of κ_ℓ exceeds that of the electrical conductivity, leading to the conjecture concerning σ/κ_ℓ mentioned above. An explicit

expression for the upper bound on ZT is also derived, which is a generalization of that previously obtained¹¹ to anisotropic systems.

This microscopic description is then applied to several materials of current interest. Sec. IV A examines bulk n-type Bi_2Te_3 , in particular, the magnitude of the induced fields, their influence on the effective electrical conductivity, and the dependence of ZT on sample orientation. $\text{HgTe}/\text{HgCdTe}$ superlattices (SLs), considered in Sec. IV B, provide an example of systems which have a tunable anisotropy. For sufficiently large anisotropy, the induced fields can be much larger than the external one. Sec. IV C focuses on isolated n-type Bi_2Te_3 quantum wells. Quantum confinement is shown to split the valley degeneracy and modify the effective masses relative to their bulk values. These effects are seen to be important in determining ZT quantitatively.

The effects of non-parabolicity in superlattices on the thermopower and Lorentz number are investigated in Sec. V. Both quantities are seen to be nearly isotropic. The thermopower is also bounded by its values along the principal axes, supporting the conjecture that optimal ZT is obtained along those directions.

II. ELECTRONIC TRANSPORT THEORY

Consider a rectangular parallelepiped sample of an anisotropic material which is placed between a hot contact at $x = 0$, temperature T_h , and a cold contact at $x = L_x$ of temperature T_c . An external electric field $\mathcal{E}^{\text{ext}} = (\mathcal{E}_{\parallel}^{\text{ext}}, 0, 0)$ is applied to drive a current from the hotter to the colder electrode. Because of the anisotropy, the resulting electric current need not be parallel to the x -direction initially; instead it may have a transverse component that leads to an accumulation of charge on the faces of the sample, resulting in an induced polarization field. Similarly, the initial thermal current through the sample need not be parallel to x , and this may lead to an induced transverse temperature gradient. In the following, we compute the effect of these induced fields and temperature gradients on the electrical conductivity, thermopower, thermal conductivity, and ZT using phenomenological linear-response theory. We assume that the transverse electrical and thermal currents vanish.

The electric current is

$$\mathbf{J}^e = \underline{\sigma}(\mathcal{E} - \underline{S}\nabla T) \equiv \underline{\sigma}\mathbf{F} \quad (1)$$

where $\underline{\sigma}$ and \underline{S} are the conductivity and Seebeck tensors respectively. Write $\mathbf{F} = (F_x, F_y, F_z) = (F_{\parallel}, \mathbf{F}_{\perp})$ with F_{\parallel} the thermoelectric field along x and \mathbf{F}_{\perp} the induced transverse fields. The conductivity tensor takes the form

$$\underline{\sigma} = \begin{pmatrix} \sigma_{\parallel} & \underline{\sigma}_{od}^T \\ \underline{\sigma}_{od} & \underline{\sigma}_{\perp} \end{pmatrix}, \quad (2)$$

where σ_{\parallel} is the component of the conductivity along the x -direction, and $\underline{\sigma}_{\perp}$ is a 2×2 tensor for the transverse y, z -directions. Since the full conductivity tensor is not block-diagonal, there will be a 2×1 off-diagonal term $\underline{\sigma}_{od}$ and its transpose.

Imposing the boundary condition $\mathbf{J}^e = (J_{\parallel}^e, 0, 0)$ on Eq. (1) corresponding to vanishing transverse current gives

$$\begin{pmatrix} J_{\parallel}^e \\ \mathbf{0} \end{pmatrix} = \underline{\sigma} \begin{pmatrix} F_{\parallel} \\ \mathbf{F}_{\perp} \end{pmatrix}. \quad (3)$$

Inserting Eq. (2) into this expression leads to a linear equation for \mathbf{F}_{\perp} with solution

$$\mathbf{F}_{\perp} = -\underline{\sigma}_{\perp}^{-1} \underline{\sigma}_{od} F_{\parallel}. \quad (4)$$

The off-diagonal elements of $\underline{\sigma}$ induce a current

$$J_{\parallel}^{\text{e,ind}} = \underline{\sigma}_{od}^T \mathbf{F}_{\perp} = -\underline{\sigma}_{od}^T \underline{\sigma}_{\perp}^{-1} \underline{\sigma}_{od} F_{\parallel} \quad (5)$$

along the x -direction. Since $\underline{\sigma}_{\perp}$ and $\underline{\sigma}_{\perp}^{-1}$ have positive eigenvalues, the quadratic form $\underline{\sigma}_{od}^T \underline{\sigma}_{\perp}^{-1} \underline{\sigma}_{od}$ is positive definite. Thus, the induced current opposes the external current $J_{\parallel}^{\text{e,ext}} = \sigma_{\parallel} F_{\parallel}$. The total current

$$J_{\parallel}^e = J_{\parallel}^{\text{e,ext}} + J_{\parallel}^{\text{e,ind}} = \sigma_1 F_{\parallel} \quad (6)$$

with

$$\sigma_1 = \sigma_{\parallel} - \underline{\sigma}_{od} \underline{\sigma}_{\perp}^{-1} \underline{\sigma}_{od} \quad (7)$$

$$= \sigma_{xx} - \sigma_{xy} \frac{\sigma_{yx} \sigma_{zz} - \sigma_{yz} \sigma_{zx}}{\sigma_{yy} \sigma_{zz} - \sigma_{yz} \sigma_{zy}} - \sigma_{xz} \frac{\sigma_{zx} \sigma_{yy} - \sigma_{zy} \sigma_{yx}}{\sigma_{yy} \sigma_{zz} - \sigma_{yz} \sigma_{zy}}. \quad (8)$$

The induced fields therefore lead to a reduced conductivity: $\sigma_1 \leq \sigma_{\parallel}$. If \underline{S} is diagonal, σ_1 is the effective conductivity; otherwise, the induced temperature gradients give rise to additional terms considered below. In the isotropic case, the induced fields vanish, and $\sigma_1 = \sigma_{\parallel}$. Note that in general $\sigma_1 \geq 0$ because

$$\sigma_1 F_{\parallel}^2 = J_{\parallel}^e F_{\parallel} = \mathbf{F}^T \cdot \mathbf{J}^e = \mathbf{F}^T \cdot \underline{\sigma} \cdot \mathbf{F} \geq 0. \quad (9)$$

The heat current \mathbf{J}^Q is given by

$$\mathbf{J}^Q = T \underline{S} \mathbf{J}^e - \underline{\kappa} \nabla T, \quad (10)$$

where $\underline{\kappa}$ is the thermal conductivity and the temperature gradient $\nabla T = (\nabla_x T, \nabla_y T, \nabla_z T) = (\nabla_{\parallel} T, \nabla_{\perp} T)$. Using the same decomposition as in Eq. (2) for $\underline{\kappa}$ and \underline{S} in Eq. (10) and setting the transverse components of the heat current to zero yields

$$\begin{pmatrix} J_{\parallel}^Q \\ \mathbf{0} \end{pmatrix} = \begin{pmatrix} T S_{\parallel} J_{\parallel}^e - \kappa_{\parallel} \nabla_{\parallel} T - \underline{\kappa}_{od}^T \nabla_{\perp} T \\ T \underline{S}_{od} J_{\parallel}^e - \underline{\kappa}_{od} \nabla_{\parallel} T - \underline{\kappa}_{\perp} \nabla_{\perp} T \end{pmatrix}. \quad (11)$$

Solving for the induced temperature gradients yields

$$\nabla_{\perp} T = \underline{\kappa}_{\perp}^{-1} (T \underline{S}_{od} J_{\parallel}^e - \underline{\kappa}_{od} \nabla_{\parallel} T). \quad (12)$$

Substituting back into Eq. (11) gives

$$J_{\parallel}^Q = T S_{\text{eff}} J_{\parallel}^e - \kappa_{\text{eff}} \nabla_{\parallel} T \quad (13)$$

with

$$\kappa_{\text{eff}} = \kappa_{\parallel} - \underline{\kappa}_{od}^T \underline{\kappa}_{\perp}^{-1} \underline{\kappa}_{od} \quad (14)$$

$$S_{\text{eff}} = S_{\parallel} - \underline{\kappa}_{od}^T \underline{\kappa}_{\perp}^{-1} \underline{S}_{od}. \quad (15)$$

Observe that σ_1 , Eq. (7), and κ_{eff} , Eq. (14), have the same form. As in the σ_1 case, the induced temperature gradients produce an induced heat current along x which opposes the external heat current $-\kappa_{\parallel} \nabla_{\parallel} T$. The net result is a reduced effective thermal conductivity: $0 \leq \kappa_{\text{eff}} \leq \kappa_{\parallel}$.

Returning to Eq. (6), we have

$$J_{\parallel}^e = \sigma_1 F_{\parallel} = \sigma_1 (\mathcal{E}_{\parallel} - S_{\parallel} \nabla_{\parallel} T - \underline{S}_{od}^T \nabla_{\perp} T). \quad (16)$$

Substituting Eq. (12) into Eq. (6) leads to

$$J_{\parallel}^e = \sigma_{\text{eff}} (\mathcal{E}_{\parallel} - S_{\text{eff}} \nabla_{\parallel} T). \quad (17)$$

with

$$\sigma_{\text{eff}} = \frac{\sigma_1}{1 + \sigma_1 T \underline{S}_{od}^T \underline{\kappa}_{\perp}^{-1} \underline{S}_{od}} \quad (18)$$

and

$$S_{\text{eff}} = S_{\parallel} - \underline{S}_{od}^T \underline{\kappa}_{\perp}^{-1} \underline{\kappa}_{od}. \quad (19)$$

From the properties of σ_1 , $0 \leq \sigma_{\text{eff}} \leq \sigma_{\parallel}$. Therefore, induced fields and temperature gradients always reduce the effective conductivity. Also, S_{eff} in Eq. (19) is the same as S_{eff} in Eq. (15) because, by the Onsager relations, $\underline{\kappa}_{\perp}$ and hence $\underline{\kappa}_{\perp}^{-1}$ are symmetric.

In the steady state, the energy-conservation equation reads

$$\nabla \cdot \mathbf{J}^Q = \mathcal{E} \cdot \mathbf{J}^e. \quad (20)$$

Using Eqs. (10) and (1), and assuming that the Thompson heat is negligible,

$$\nabla \cdot \mathbf{J}^Q = \nabla \cdot (T \underline{S} \mathbf{J}^e - \underline{\kappa} \nabla T) = \nabla T \underline{S} \mathbf{J}^e - \nabla \cdot (\underline{\kappa} \nabla T) \quad (21)$$

and

$$\mathcal{E} \cdot \mathbf{J}^e = \mathbf{J}^e (\underline{\sigma}^{-1} \mathbf{J}^e + \underline{S} \nabla T) = \mathbf{J}^e \underline{\sigma}^{-1} \mathbf{J}^e + \mathbf{J}^e \underline{S} \nabla T. \quad (22)$$

Thus, Eq. (20) becomes

$$\mathbf{J}^e \underline{\sigma}^{-1} \mathbf{J}^e + \nabla \cdot (\underline{\kappa} \nabla T) = 0. \quad (23)$$

Since $\mathbf{J}^e = (J_{\parallel}^e, 0, 0)$, the first term is $(\underline{\sigma}^{-1})_{11} J_{\parallel}^{e2} = (\det \underline{\sigma}_{\perp} / \det \underline{\sigma}) J_{\parallel}^{e2} = \sigma_{\perp}^{-1} J_{\parallel}^{e2}$. The last step is justified by expanding the determinants and comparing to Eq. (8). With $\nabla T = (\nabla_{\parallel} T, \nabla_{\perp} T)$ and using Eq. (12), the second term is

$$\nabla \cdot \begin{pmatrix} \kappa_{\parallel} \nabla_{\parallel} T + \underline{\kappa}_{od}^T \nabla_{\perp} T \\ \underline{\kappa}_{od} \nabla_{\parallel} T + \underline{\kappa}_{\perp} \nabla_{\perp} T \end{pmatrix} = \nabla \cdot \begin{pmatrix} (\kappa_{\parallel} - \underline{\kappa}_{od}^T \underline{\kappa}_{\perp}^{-1} \underline{\kappa}_{od}) \nabla_{\parallel} T + \underline{\kappa}_{od}^T \underline{\kappa}_{\perp}^{-1} \underline{S}_{od} T J_{\parallel}^e \\ T \underline{S}_{od} J_{\parallel}^e \end{pmatrix} \quad (24)$$

$$= \kappa_{\text{eff}} \nabla_{\parallel}^2 T + \underline{S}_{od}^T \underline{\kappa}_{\perp}^{-1} \underline{S}_{od} T J_{\parallel}^{e2}. \quad (25)$$

Therefore Eq. (20) reduces to

$$\sigma_{\text{eff}}^{-1} J_{\parallel}^{e2} + \kappa_{\text{eff}} \nabla_{\parallel}^2 T = 0. \quad (26)$$

With the help of Eqs. (17), (13) and (26), the thermoelectric figure of merit becomes

$$ZT = T \sigma_{\text{eff}} S_{\text{eff}}^2 / \kappa_{\text{eff}}. \quad (27)$$

The transport coefficients are simply replaced by their effective versions.

These results are derived more succinctly using a general formalism based directly on the Onsager coefficients in Appendix A. Rigorous bounds can be placed on the magnitude and sign of σ_{eff} and κ_{eff} , but not on S_{eff} without introducing a microscopic model that relates these transport coefficients. The next Section considers an example of such a model.

III. MICROSCOPIC MODEL: PARABOLIC BANDS

A. Three-Dimensional Structures

According to semiclassical transport theory, the Boltzmann equation in the relaxation-time approximation yields the transport coefficients

$$\sigma_{ij} = e^2 \int d\varepsilon (-\partial f_0 / \partial \varepsilon) \Sigma_{ij}(\varepsilon) \quad (28)$$

$$T(\sigma \cdot S)_{ij} = e \int d\varepsilon (-\partial f_0 / \partial \varepsilon) \Sigma_{ij}(\varepsilon) (\varepsilon - \mu) \quad (29)$$

$$T \kappa_{0,ij} = \int d\varepsilon (-\partial f_0 / \partial \varepsilon) \Sigma_{ij}(\varepsilon) (\varepsilon - \mu)^2, \quad (30)$$

where f_0 is the Fermi-Dirac distribution $f_0(\varepsilon) = 1/(\exp((\varepsilon - \mu)/k_B T) + 1)$, μ the chemical potential, and

$$\Sigma_{ij}(\varepsilon) = \int \frac{2d^3 \mathbf{k}}{(2\pi)^3} v_i(\mathbf{k}) v_j(\mathbf{k}) \tau(\mathbf{k}) \delta(\varepsilon - \varepsilon(\mathbf{k})) \quad (31)$$

are the components of the transport distribution tensor, the generalization of the function discussed by Mahan and Sofo.¹¹ Here $\varepsilon(\mathbf{k})$ is the electronic dispersion relation, $v_i(\mathbf{k}) = \hbar^{-1} \partial \varepsilon(\mathbf{k}) / \partial k_i$ the electronic group velocity, and $\tau(\mathbf{k})$ the relaxation time. Note that $\underline{\kappa}_0$ is the electronic thermal conductivity at zero electrochemical potential gradient

inside the sample;¹¹ the usual electronic thermal conductivity at zero electric current, $\underline{\kappa}_e$, is given in terms of $\underline{\kappa}_0$ by $\underline{\kappa}_e = \underline{\kappa}_0 - T\sigma\underline{S}^2$.

The microscopic model to be used here assumes the conduction to be taking place in a single parabolic band having N degenerate valleys centered at $\mathbf{k}^{(n)}$, $n = 1, \dots, N$ respectively. The dispersion relation for each valley is

$$\varepsilon^{(n)}(\mathbf{k}) = \varepsilon_0 + (\hbar^2/2) \sum_{i,j} (k_i - k_i^{(n)}) M_{ij}^{(n)-1} (k_j - k_j^{(n)}) \quad (32)$$

with $\underline{M}^{(n)-1}$ the inverse effective-mass tensor. The corresponding group velocity is

$$v_i^{(n)}(\mathbf{k}) = \hbar^{-1} \partial \varepsilon(\mathbf{k}) / \partial k_i = \hbar \sum_j M_{ij}^{(n)-1} (k_j - k_j^{(n)}). \quad (33)$$

Intervalley scattering will be neglected. Thus the transport distribution tensor involves just a sum over the N valleys. Assuming the relaxation time to be a function of energy alone, $\tau(\mathbf{k}) = \tau(\varepsilon(\mathbf{k}))$, and independent of crystal orientation,

$$\Sigma_{ij}(\varepsilon) = \tau(\varepsilon) \sum_{n=1}^N \int \frac{2d^3\mathbf{k}}{(2\pi)^3} \hbar^2 \sum_{i',j'} M_{ii'}^{(n)-1} k_{i'} M_{jj'}^{(n)-1} k_{j'} \delta(\varepsilon - \varepsilon(\mathbf{k} + \mathbf{k}^{(n)})) \quad (34)$$

$$= \tau(\varepsilon) \hbar^2 \sum_{n=1}^N \sum_{i',j'} M_{ii'}^{(n)-1} M_{jj'}^{(n)-1} \int k_{i'} k_{j'} \delta(\varepsilon - \mathbf{k} \underline{X}^{(n)} \mathbf{k}) \frac{2d^3\mathbf{k}}{(2\pi)^3} \quad (35)$$

$$= \frac{2\tau(\varepsilon) \hbar^2}{(2\pi)^3} \sum_{n=1}^N \sum_{i',j'} M_{ii'}^{(n)-1} M_{jj'}^{(n)-1} \left[-\frac{\partial}{\partial X_{i'j'}} \int \Theta(\varepsilon - \mathbf{k} \underline{X}^{(n)} \mathbf{k}) d^3\mathbf{k} \right] \quad (36)$$

$$= \frac{2^{3/2} \tau(\varepsilon) \varepsilon^{3/2}}{3\pi^2 \hbar^3} \sum_{n=1}^N \sqrt{\det \underline{M}^{(n)}} M_{ij}^{(n)-1}, \quad (37)$$

where $X_{ij}^{(n)}$ are the components of $\underline{X}^{(n)} = (\hbar^2/2) \underline{M}^{(n)-1}$. This transformation relies explicitly on the validity of the effective-mass approximation, the neglect of intervalley scattering, and the relaxation-time approximation used here. The square bracket in Eq. (36) is evaluated using the identity

$$\frac{\partial}{\partial X_{ij}^{(n)}} \det \underline{X}^{(n)} = (\det \underline{X}^{(n)}) X_{ij}^{(n)-1} \quad (38)$$

and the change of variable $\mathbf{k}' = \sqrt{\underline{X}^{(n)}} \mathbf{k}$. Thus,

$$\underline{\Sigma}(\varepsilon) = \underline{A} \mathcal{T}(\varepsilon) \quad (39)$$

with

$$\underline{A} = \sum_{n=1}^N \left(m_0^{-1/2} \sqrt{\det \underline{M}^{(n)}} \right) \underline{M}^{(n)-1} \quad (40)$$

and

$$\mathcal{T}(\varepsilon) = \frac{2^{3/2} m_0^{1/2}}{3\pi^2 \hbar^3} \varepsilon^{3/2} \tau(\varepsilon). \quad (41)$$

The constant, dimensionless matrix \underline{A} contains the full tensorial structure and separates it from the energy dependence in $\mathcal{T}(\varepsilon)$.

The conductivity then becomes

$$\underline{\sigma} = e^2 \int d\varepsilon (-\partial f_0 / \partial \varepsilon) \mathcal{T}(\varepsilon) \underline{A} \equiv \sigma_0 \underline{A}. \quad (42)$$

Since

$$\underline{(\sigma \cdot S)} = (e/T) \int d\varepsilon (-\partial f_0/\partial \varepsilon) \mathcal{T}(\varepsilon) (\varepsilon - \mu) \underline{A} \equiv \underline{A} \sigma_0 S_0, \quad (43)$$

$$\underline{S} = \underline{\sigma}^{-1} \underline{(\sigma \cdot S)} = S_0 \underline{1}. \quad (44)$$

The Seebeck tensor is therefore necessarily *isotropic*. Further,

$$\underline{\kappa}_0 = \underline{A} \kappa_0 \quad (45)$$

with

$$\kappa_0 = T^{-1} \int d\varepsilon (-\partial f_0/\partial \varepsilon) \mathcal{T}(\varepsilon) (\varepsilon - \mu)^2. \quad (46)$$

The zero-current electronic thermal conductivity becomes

$$\underline{\kappa}_e = \underline{\kappa}_0 - T \underline{\sigma} \underline{S}^2 \equiv \underline{A} \kappa_e \quad (47)$$

for $\kappa_e = \kappa_0 - T \sigma_0 S_0^2$.

These results lead to the following surprising conclusion: When the lattice thermal conductivity is neglected, then, within the effective-mass approximation as specified here, the thermoelectric figure of merit ZT is independent of the sample orientation. Note that

$$\underline{\kappa}_e \cdot \underline{\sigma}^{-1} = \underline{A} \kappa_e \cdot \underline{A}^{-1} / \sigma_0 = (\kappa_e / \sigma_0) \underline{1} \equiv L_0 T \underline{1}, \quad (48)$$

where the Lorentz number $L_0 = \kappa_e / \sigma_0 T$. Thus, $\kappa_{e,ij} = L_0 T \sigma_{ij}$ and

$$\kappa_{\text{eff}} = L_0 T \sigma_{\text{eff}} \quad (49)$$

as expected. Finally, since \underline{S} is isotropic, $S_{\text{eff}} = S_0$. Combining these effective transport coefficients yields

$$ZT = T \sigma_{\text{eff}} S_{\text{eff}}^2 / \kappa_{\text{eff}} = S_0^2 / L_0, \quad (50)$$

a constant independent of direction.

B. Lower-dimensional Structures

Dimensionality enters the transport coefficients through the \mathbf{k} -space integrals

$$d^3 k \quad \leftrightarrow \quad (2\pi/L_z) d^2 k \quad \leftrightarrow \quad ((2\pi)^2/L_y L_z) dk \quad (51)$$

for three, two or one dimensions respectively, where L_y and L_z are the sample sizes in the y - and z -directions. Dimensionality also enters through the confinement energies and effective masses for carriers constrained to move in a lower-dimensional device.

For the two-dimensional case with $\mathcal{E} = (\mathcal{E}_x^{\text{ext}}, \mathcal{E}_y^{\text{ind}})$ and $\nabla T = (\nabla_x T, \nabla_y T)$, the induced fields are given by Eqs. (4) and (12), the transport coefficients by Eqs. (14), (15), and (18) with $\underline{\sigma}_\perp$ replaced by σ_{yy} , $\underline{\sigma}_{od}$ replaced by σ_{yx} ; similarly for the other transport coefficients. The analogue of Eq. (31) for the components of the transport distribution tensor is obtained within the effective-mass approximation using Eq. (51):

$$\Sigma_{ij}(\varepsilon) = \frac{2\tau(\varepsilon)\hbar^2}{4\pi^2 L_z} \sum_{n=1}^N \sum_{i'j'} M_{ii'}^{(n)-1} M_{jj'}^{(n)-1} \int d^2 \mathbf{k} k_{i'} k_{j'} \delta(\varepsilon - \mathbf{k} \underline{X}^{(n)} \mathbf{k}). \quad (52)$$

This expression has the same form as Eq. (39) with

$$\underline{A} = \sum_{n=1}^N \sqrt{\det \underline{M}^{(n)}} \underline{M}^{(n)-1} \quad (53)$$

and

$$\mathcal{T}(\varepsilon) = \varepsilon\tau(\varepsilon)/\pi\hbar^2L_z. \quad (54)$$

These equations are to be contrasted with Eqs. (40) and (41) for the three-dimensional case. Thus, analogously to Eqs. (42), (44), and (47), $\underline{\sigma} = \underline{A}\sigma_0$, $\underline{S} = S_0\underline{1}$ and $\underline{\kappa}_e = \underline{A}\kappa_e$ where the two-dimensional \underline{A} and $\mathcal{T}(\varepsilon)$ must be used in defining σ_0 , S_0 and κ_0 . Finally, $\underline{\kappa}_e\underline{\sigma}^{-1} = L_0T\underline{1}$ so that

$$\kappa_{\text{eff}} = L_0T\sigma_{\text{eff}}. \quad (55)$$

Also, $S_{\text{eff}} = S_0$ because \underline{S} is isotropic in two dimensions as well. The corresponding figure of merit

$$ZT = T\sigma_{\text{eff}}S_{\text{eff}}^2/\kappa_{\text{eff}} = S_0^2/L_0 \quad (56)$$

is again independent of direction, as in three dimensions.

It is seen that the two-dimensional and three-dimensional results are entirely analogous and that the former are obtained from the latter by taking the limit as one of the effective masses tends to infinity. In this limit, the ellipsoidal surface in \mathbf{k} -space of constant energy becomes increasingly prolate, until it reaches the edge of the Brillouin zone, after which it assumes a cylindrical shape extending from $-\pi/L_z$ to π/L_z upon further increase in the effective-mass parameter. Furthermore ZT in two dimensions can be enhanced due to the factor of $1/L_z$ in the density of states, which, as pointed out in Ref. 1, becomes large for small thicknesses.

In the one-dimensional case there is no transport in the transverse direction. Thus there are no transverse fields and the microscopic and effective transport coefficients are the same. Moreover, all transport coefficients are scalars. The transport distribution function is found to be

$$\Sigma(\varepsilon) = \sum_{n=1}^N \frac{2}{\pi L_y L_z} \sqrt{\frac{2\varepsilon}{\hbar^2 m_x^{(n)}}} \tau(\varepsilon). \quad (57)$$

Just as in two dimensions, the $1/L_y L_z$ factor leads to an enhancement of the density of states and thus of ZT for thin wires.⁹ (The wire becomes approximately one-dimensional when it is thin enough that the confinement energy places all states associated with its three-dimensional structure sufficiently high in energy that they do not contribute.)

C. Implications for ZT

We shall now derive an upper bound for ZT of the Sofo and Mahan form¹¹ and show that the highest conductivity direction gives optimal values for ZT . The inclusion of an isotropic lattice thermal conductivity κ_ℓ causes ZT to lose its isotropy.

The figure of merit including an isotropic lattice thermal conductivity $\underline{\kappa}_\ell = \kappa_\ell\underline{1}$ may be written in the form

$$ZT = T\sigma_{\text{eff}}S_{\text{eff}}^2/\kappa_{\text{eff}} \quad (58)$$

where σ_{eff} and S_{eff} are as in Sec. II. $\kappa_{\text{eff}} = \kappa_e^* + \kappa_\ell$ with

$$\begin{aligned} \kappa_e^* = & \kappa_{e,xx} - \kappa_{e,xy} \frac{\kappa_{e,yx}(\kappa_{e,zz} + \kappa_\ell) - \kappa_{e,yz}\kappa_{e,zx}}{(\kappa_{e,yy} + \kappa_\ell)(\kappa_{e,zz} + \kappa_\ell) - \kappa_{e,yz}\kappa_{e,zy}} \\ & - \kappa_{e,xz} \frac{\kappa_{e,zx}(\kappa_{e,yy} + \kappa_\ell) - \kappa_{e,zy}\kappa_{e,yx}}{(\kappa_{e,yy} + \kappa_\ell)(\kappa_{e,zz} + \kappa_\ell) - \kappa_{e,yz}\kappa_{e,zy}}. \end{aligned} \quad (59)$$

defining the electronic thermal conductivity in the presence of the non-vanishing κ_ℓ and the sample boundaries. As shown in Appendix B, the upper bound on ZT is given by

$$ZT \leq a_0(\kappa_0/\kappa_\ell). \quad (60)$$

The dimensionless quantity a_0 is defined by Eq. (B2). In the isotropic case,¹¹ $a_0 = 1$; in the present case, a_0 is of order unity. The maximum value of ξ defined in Ref. 11 and in Appendix B [Eq. (B12)] of unity is attained if and only if $\mathcal{T}(\varepsilon)$ is proportional to a δ -function. In the more physical case $\mathcal{T}(\varepsilon) \propto \varepsilon^r$ with r varying between -0.5 and 2, numerical computations show that ξ tends to 1 as $\mu/k_B T \rightarrow -\infty$ and to zero as $\mu/k_B T \rightarrow \infty$. For $\mu/k_B T = 0$, ξ ranges from 0.5 to 0.8. Thus, the upper bound can be reached at the cost of going to low carrier concentrations, whereas higher carrier concentrations imply smaller ξ . The optimum concentration lies somewhere in between.

We now show that, in the effective-mass, relaxation-time, no intervalley scattering, and isotropic-thermal-conductivity approximations, ZT is highest in the direction of maximum electrical conductivity. In the anisotropic case, σ_{eff} and κ_{eff} have an angular dependence obtained in the frame of the sample by a rotation from their common principal frame. S_{eff} does not because in our microscopic model \underline{S} is isotropic. ZT is therefore also anisotropic. Let now \underline{P} be any symmetric and positive matrix and $\lambda \geq 0$ a positive number; then by the properties of positive matrices, $\underline{P}^{-1} \geq (\underline{P} + \lambda \underline{1})^{-1}$. For the application to thermoelectrics let

$$\underline{\kappa}_e = \begin{pmatrix} \kappa_{\parallel} & \underline{\kappa}_{od}^T \\ \underline{\kappa}_{od} & \underline{\kappa}_{\perp} \end{pmatrix}. \quad (61)$$

In analogy with Eq. (14) we find

$$\kappa_e^* = \kappa_{\parallel} - \underline{\kappa}_{od}^T (\underline{\kappa}_{\perp} + \kappa_{\ell} \underline{1})^{-1} \underline{\kappa}_{od}. \quad (62)$$

Taking $\underline{P} = \underline{\kappa}_{\perp}$ and $\lambda = \kappa_{\ell}$, the relation $\underline{P}^{-1} \geq (\underline{P} + \lambda \underline{1})^{-1}$ shows that

$$\underline{\kappa}_{od}^T (\underline{\kappa}_{\perp} + \kappa_{\ell} \underline{1})^{-1} \underline{\kappa}_{od} \leq \underline{\kappa}_{od}^T \underline{\kappa}_{\perp}^{-1} \underline{\kappa}_{od}. \quad (63)$$

Thus, for any κ_{ℓ}

$$\kappa_e^*(\kappa_{\ell}) \geq \kappa_e^*(\kappa_{\ell} = 0) = (\kappa_e / \sigma_0) \sigma_{\text{eff}}. \quad (64)$$

This shows that the ratio $\kappa_e^* / \sigma_{\text{eff}}$ is minimized when the axis of current flow in steady state lies along one of the principal directions, where, whatever the value of κ_{ℓ} , the induced-field related terms vanish and so equality obtains in Eq. (64). Writing ZT in the form

$$ZT = \frac{S_0^2}{\kappa_e^* / T \sigma_{\text{eff}} + \kappa_{\ell} / T \sigma_{\text{eff}}}, \quad (65)$$

the second term in the denominator is seen to be smallest along the principal direction with largest electrical conductivity and therefore ZT is maximized for current flow along this direction.

On the other hand, for a sufficiently anisotropic lattice thermal conductivity the favored direction might be determined by its minimum rather than that of the highest electrical conductivity. For crystals in which two of the principal values of the electrical conductivity are equal, such as Bi_2Te_3 and SLs, numerical results show that as long as the anisotropy of $\underline{\kappa}_{\ell}$ is smaller than that of $\underline{\sigma}$, the optimum ZT is still to be found in the direction of greatest electrical conductivity. This suggests that, generally speaking, the figure of merit will be maximized in the principal crystal direction in which the ratio $\sigma_i / \kappa_{\ell,i}$ is greatest, where σ_i and $\kappa_{\ell,i}$ are the principal values of the electrical and lattice thermal conductivity tensors obtained from summing over valleys.

IV. APPLICATIONS

In the Section, the formalism of Sec. III is applied to several systems in which the effective-mass approximation is valid and for which, as shown above, the thermopower is isotropic.

A. Bulk Bi_2Te_3

Bismuth telluride is a semiconductor with a room-temperature energy gap of 0.13 eV that crystallizes in a trigonal structure with space group D_{3d}^5 ($R\bar{3}m$).¹² An orthogonal coordinate system can be defined in this structure, consisting of the trigonal (three-fold rotation) axis, a bisectrix axis that resides within a reflection plane and is normal to the trigonal axis, and a binary axis which is along the two-fold rotation axis orthogonal to the other two directions. This coordinate system will be used throughout the paper and will be referred to as the crystal frame.

As shown in Fig. 1, the constant-energy surfaces of the conduction band at low doping are ellipsoidal. There are six degenerate valleys, each described by a highly anisotropic effective-mass tensor.¹³ As illustrated in the figure, two of these valleys are bisected by the trigonal-bisectrix plane and their principal axes are rotated approximately 1.2° from the bisectrix axis. The light effective masses are $m_1 = 0.025m_0$ near the bisectrix, $m_2 = 0.26m_0$ along the binary axis and $m_3 = 0.19m_0$ near the trigonal axis. These two surfaces are related to each other by inversion through the origin.

The remaining four constant-energy surfaces are obtained from the first two by rotations through $\pm 2\pi/3$ about the trigonal axis.

The tensorial transport distribution function, Eq. (39), involves the scalar part $\mathcal{T}(\varepsilon)$ given by Eq. (41). The relaxation time $\tau(\varepsilon)$ taken to be independent of energy and is determined from the experimental mobility along the bisectrix, $1200 \text{ cm}^2 / \text{V s}$.¹³ The matrix part \underline{A} is constructed from the experimentally derived inverse mass matrix for a single conduction band ellipsoid ($n = 1$).¹³ Application of the point group operations of the crystal give the other inverse mass matrices needed to construct \underline{A} in the crystal frame [cf. Eq. (40)], which is then transformed into the frame of the sample. ZT is obtained from the resulting transport coefficients by taking the lattice thermal conductivity at 300 K to be 1.5 W / m K (Ref. 13) and isotropic. We shall assume a carrier density $n = 5.2 \times 10^{18} \text{ cm}^{-3}$, which gives the maximal $ZT = 0.71$ in our model when the sample is cut along the bisectrix.

The magnitude of the induced fields in a crystal cut at an angle θ with respect to the trigonal axis in the trigonal-bisectrix plane is plotted in Fig. 2(a). The induced field vanishes when the sample is cut along either the bisectrix or the trigonal directions. This field reaches its maximum of 76% of the external field for a sample cut 0.36π radians with respect to the trigonal axis. As discussed in Sec. II, an external temperature gradient may induce temperature gradients along the transverse faces. The induced gradients are at most 12% of the external gradient and have little effect on ZT .

The effective electrical conductivity σ_{eff} [Eq. (18)] is shown in Fig. 2(b). As the direction in which the sample is cut is changed from the bisectrix ($\theta = \pi/2$) to the trigonal ($\theta = 0$), the conductivities computed with (σ_{eff}) and without (σ_{xx}) sample boundary effects are both reduced by a factor of four due to the intrinsic anisotropy of the material. σ_{eff} is further reduced with respect to σ_{xx} by the induced fields when the sample is oriented along low-symmetry directions by as much as 60%. The influence of the sample boundaries is therefore substantial.

The combination of intrinsic anisotropy and the effects of the induced fields also affect ZT , but only if κ_ℓ is non-zero. As shown in Fig. 3(a) for a hypothetical material with $\kappa_\ell = 0$, $ZT = 2.6$ and is isotropic [Eq. (50)]. As seen in Fig. 3(b), when κ_ℓ assumes its bulk value, ZT becomes anisotropic and decreases to a maximum value of 0.71. The maximal ZT applies to samples cut along the high-conductivity bisectrix-binary plane, consistent with the results of Sec. III C. The minimal $ZT = 0.22$ occurs for samples cut along the low-conductivity trigonal axis. Despite the complicated many-valley band structure, ZT is independent of the azimuthal angle ϕ defined in the inset to Fig. 3(a). This is consistent with a group-theoretical analysis and is suggested by the relative orientations of the ellipsoids in Fig. 1.

Introducing anisotropy into κ_ℓ by increasing its value along the bisectrix reduces ZT for samples cut along this direction, but not for those cut along the trigonal axis. When the ratio σ/κ_ℓ along the trigonal axis exceeds that along the bisectrix, the maximal ZT shifts to the low-conductivity trigonal direction. ZT is never maximal along a low-symmetry direction. These numerical results support the conjecture at the end of Sec. III C.

B. HgTe/HgCdTe Superlattices

We now consider HgTe/HgCdTe SLs, one of many SLs whose well and barrier materials have direct Γ -point band gaps. The constant energy surfaces of the lowest conduction subband $C1$ consist of single ellipsoids of revolution aligned with the growth axis of the SL. The conductivity will typically be a minimum along the growth axis (σ_{min}) and a maximum within the SL plane (σ_{max}). If the sample is cut at an angle ϕ relative to the SL planes, the induced fields will be non-zero only for the faces intersected by the SL growth axis, as indicated in the inset to Fig. 4. Use of Eq. (4) then yields the relative magnitude of the induced electric field as

$$\frac{\mathcal{E}^{\text{ind}}}{F^{\text{ext}}} = \frac{(\sigma_{\text{max}} - \sigma_{\text{min}}) \sin \phi \cos \phi}{\sigma_{\text{max}} \sin^2 \phi + \sigma_{\text{min}} \cos^2 \phi}. \quad (66)$$

This relation is plotted in Fig. 4 for several values of the ratio $\sigma_{\text{min}}/\sigma_{\text{max}}$. When the system is isotropic, $\sigma_{\text{min}}/\sigma_{\text{max}} = 1$ and the induced field vanishes. With increasing anisotropy, \mathcal{E}^{ind} becomes non-zero away from the high-symmetry growth and in-plane orientations and peaks at an angle

$$\phi_{\text{max}} = \sin^{-1} \sqrt{\sigma_{\text{min}}/(\sigma_{\text{max}} + \sigma_{\text{min}})}. \quad (67)$$

The maximum induced field is

$$\mathcal{E}^{\text{ind}}/F^{\text{ext}}|_{\text{max}} = (\sigma_{\text{max}} - \sigma_{\text{min}})/2\sqrt{\sigma_{\text{max}}\sigma_{\text{min}}}. \quad (68)$$

In the limit $\sigma_{\text{min}}/\sigma_{\text{max}} \ll 1$, these relations reduce to $\phi_{\text{max}} \sim \sqrt{\sigma_{\text{min}}/\sigma_{\text{max}}}$ and $\mathcal{E}^{\text{ind}}/F^{\text{ext}}|_{\text{max}} \sim (1/2)\sqrt{\sigma_{\text{max}}/\sigma_{\text{min}}}$. Thus, as illustrated in Fig. 4, a relative induced field much larger than unity is obtained for sufficiently small $\sigma_{\text{min}}/\sigma_{\text{max}}$.

From Eq. (68), the maximal induced field exceeds the external one when $\sigma_{\min}/\sigma_{\max} \leq 3 - 2\sqrt{2} \cong 0.172$. This geometrical effect may be practically useful.

As specific examples, consider two superlattices: (1) 30-Å HgTe / 20-Å Hg_{0.15}Cd_{0.85}Te and (2) 20-Å HgTe / 40-Å Hg_{0.15}Cd_{0.85}Te. Realistic band structures for these materials are obtained through an 8-band $\mathbf{K} \cdot \mathbf{p}$ theory within the envelope function approximation¹⁴ based on the parameters in Tab. I. Application of this approach to other II-VI and III-V SLs yields accurate band structures which reproduce experimental optical absorption spectra with no adjustable parameters.¹⁴ The masses of the $C1$ subband along the growth and in-plane directions required for the transport calculations are given in Tab. II. The room-temperature energy gaps are seen to satisfy $E_g \geq 10k_B T$ in both structures, so hole conduction is negligible. Transport in the next highest conduction subband is also negligible, since it lies more than $20k_B T$ higher in energy than $C1$ in both SLs. The relaxation time and lattice thermal conductivity enter ZT significantly only in the ratio $\kappa_\ell/\sigma_{\text{eff}}T$ [Eq. (65)]. Their values are estimated from those of an alloy of the same composition as the SL (Tab. II). Thus, interface scattering is neglected.

The thermoelectric performance of these SLs is shown in Tab. II. Since $\sigma_{\min}/\sigma_{\max} = m_{\parallel}/m_{\perp}$, SL (1)'s 0.66 mass ratio between the in-plane and growth directions yields a maximum induced field of only $0.2F^{\text{ext}}$. SL (2)'s much smaller 0.39 mass ratio, indicating a larger anisotropy, yields a correspondingly larger induced field of $0.5F^{\text{ext}}$. For even larger anisotropies, the effective mass approximation breaks down, but estimates using the band structure of Sec. V suggest that induced fields up to $17F^{\text{ext}}$ can be obtained in a 40-Å HgTe / 50-Å CdTe SL. As for bulk Bi₂Te₃, induced temperature gradients are small, at most 2% of the external gradient for SL (1) and SL (2). Note that the maximal ZT s shown in Tab. II, although small in magnitude, represent a substantial increase over the equivalent bulk alloy.

C. Bi₂Te₃ Quantum Wells

Consider a quantum well formed from a multi-valley semiconductor. Within the single-band envelope function approximation,¹⁵ the wave function for the n th valley, $\psi^{(n)}(\mathbf{r})$, satisfies

$$\left[- \sum_{ij} \alpha_{ij}^{(n)} \partial_i \partial_j + V(\mathbf{r}) \right] \psi^{(n)}(\mathbf{r}) = E^{(n)} \psi^{(n)}(\mathbf{r}), \quad (69)$$

where $\alpha_{ij} = (\hbar^2/2)M_{ij}^{(n)-1}$ is proportional to the bulk inverse effective mass tensor $M_{ij}^{(n)-1}$, $E^{(n)}$ the energy measured from the bottom of the valley in the bulk, and $i, j = x, y, \text{ or } z$. $V(\mathbf{r})$ is the confining potential, which is taken to be a square well of width L_z and infinite height. Solution of Eq. (69) yields the eigenfunctions

$$\psi_m^{(n)}(\mathbf{r}) = \sqrt{2/L_z} \exp \left[i \left(k_x x + k_y y - (\alpha_{zx}^{(n)} k_x + \alpha_{zy}^{(n)} k_y) z / \alpha_{zz}^{(n)} \right) \right] \sin(m\pi z / L_z) \quad (70)$$

and the eigenenergies

$$E_m^{(n)}(k_x, k_y) = \sum_{i,j=x,y} k_i \alpha_{ij}^{(n)\text{Well}} k_j + E_m^{(n)\text{Conf}} \quad (71)$$

with

$$\alpha_{ij}^{(n)\text{Well}} = \begin{pmatrix} \alpha_{xx}^{(n)} - \alpha_{xz}^{(n)} \alpha_{zx}^{(n)} / \alpha_{zz}^{(n)} & \alpha_{xy}^{(n)} - \alpha_{xz}^{(n)} \alpha_{zy}^{(n)} / \alpha_{zz}^{(n)} \\ \alpha_{yx}^{(n)} - \alpha_{yz}^{(n)} \alpha_{zx}^{(n)} / \alpha_{zz}^{(n)} & \alpha_{yy}^{(n)} - \alpha_{yz}^{(n)} \alpha_{zy}^{(n)} / \alpha_{zz}^{(n)} \end{pmatrix} \quad (72)$$

and the confinement energy

$$E_m^{(n)\text{Conf}} = \alpha_{zz}^{(n)} \pi^2 m^2 / L_z^2, \quad (73)$$

for $m = 1, 2, 3, \dots$

Thus, the quantum well band structure differs from that of the bulk in two ways. First, the energy of the bottom of the n th valley is shifted with respect to the bulk by an amount $E_1^{(n)\text{Conf}}$ that is inversely proportional to $m_{zz}^{(n)}$. Since $m_{zz}^{(n)}$ is generally different for different n , the confinement splits the valley degeneracy. If the well is sufficiently narrow, only the valleys having the lowest confinement energy will contribute to the transport. Second, as seen from Eq. (72), the masses in the quantum well differ from those in the bulk by terms second order in the off-diagonal elements of the bulk inverse effective-mass tensor.

Suppose the well material is n-type Bi₂Te₃. The bulk band structure was described in Sec. IV A. The relaxation time and lattice thermal conductivity can be obtained as in Ref. 1, which neglects interface effects. Eqs. (72), (39), and (53)-(54) then lead directly to the transport coefficients and ZT . For simplicity, κ_ℓ of the barriers is neglected. Thus, ZT is an overestimate.^{2,16}

Examine two orientations of the quantum well: one in which the growth direction is along the trigonal axis and one in which it is along the binary. In both cases, take the currents to flow along the bisectrix. These choices are expected to yield the best ZT s, since the currents are along the bulk high-conductivity direction and the alignment of the well with the crystal axes eliminates detrimental induced fields. The maximal ZT for these configurations is plotted as a function of well width in Fig. 5.

As seen in this figure, quantum well growth along the trigonal axis yields larger ZT s. From Fig. 1, the masses of each ellipsoid along the trigonal axis are the same, but they differ along the binary axis. Thus, all six ellipsoids contribute to transport in wells grown along the trigonal axis, but valley splitting allows only two ellipsoids to contribute in wells grown along the binary axis. The resulting larger density of states in the former case leads to higher ZT s. For a given orientation, the density of states is also larger for smaller well widths, resulting in an increase of ZT with decreasing well widths in both orientations.¹

For comparison, Fig. 5 also shows ZT computed using the simpler Bi₂Te₃ band structure of Ref. 1. This band structure consists of six equivalent ellipsoids whose principal axes are all aligned with those of the crystal. As in the multi-ellipsoid model, ZT is larger for wells grown along the trigonal axis and for smaller well widths. However, the magnitude of ZT is larger than in the multi-ellipsoid model. This difference arises because each ellipsoid shares the same orientation, allowing all of the ellipsoids' low-mass directions to lie along the bisectrix and preventing any valley splitting.

V. MICROSCOPIC MODEL: NON-PARABOLIC BANDS

Within the effective-mass approximation, the analysis of Sec. III showed that the thermopower and Lorentz number are isotropic. To see how a non-parabolic band structure affects these conclusions, consider an electronic dispersion relation of the Esaki-Tsu form:¹⁷

$$\varepsilon(\mathbf{k}) = \hbar^2 k_{\parallel}^2 / 2m_{\parallel} + \Delta(1 - \cos k_z d) \quad (74)$$

with wave vector $\mathbf{k} = (k_{\parallel} \cos \varphi, k_{\parallel} \sin \varphi, k_z)$. This relation models a superlattice of period d . The in-plane dispersion is parabolic with mass m_{\parallel} , and that along the growth direction has a tight-binding form with band width $2\Delta = (\varepsilon(0, 0, \pi/d) - \varepsilon(0, 0, 0))$. Since the mass along the growth direction $m_z = \hbar^2 / \Delta d^2$, the anisotropy can be increased by reducing Δ .

In the principal frame of the SL, the transport distribution tensor [Eq. (31)] is diagonal with components

$$\Sigma_{\text{Growth}}(\varepsilon) = \frac{m_{\parallel} d \tau(\varepsilon)}{2\pi^2 \hbar^4} \begin{cases} \Delta^2 \cos^{-1}(1 - \varepsilon/\Delta) + (\varepsilon - \Delta) \sqrt{\varepsilon(2\Delta - \varepsilon)}, & \varepsilon < 2\Delta \\ \pi \Delta^2, & \varepsilon \geq 2\Delta \end{cases} \quad (75)$$

along the growth direction and

$$\Sigma_{\text{In-plane}}(\varepsilon) = \frac{\tau(\varepsilon)}{\pi^2 \hbar^2 d} \begin{cases} (\varepsilon - \Delta) \cos^{-1}(1 - \varepsilon/\Delta) + \sqrt{\varepsilon(2\Delta - \varepsilon)}, & \varepsilon < 2\Delta \\ \pi(\varepsilon - \Delta), & \varepsilon \geq 2\Delta \end{cases} \quad (76)$$

along the planes. The transport coefficients are obtained from Eqs. (28)-(30) in the principal frame and then transformed into the sample frame. As in Sec. III, the relaxation time $\tau(\mathbf{k})$ is assumed to be a function of energy only. Direct computation with $\tau \propto \varepsilon^r$ indicates that the qualitative features discussed below are independent of the choice of r . Quantitatively, the thermopower is an approximately linear function of r at fixed sample orientation and chemical potential μ and increases by approximately 50% as r goes from 0 to 1.5. In what follows, $r = 0$, $d = 100 \text{ \AA}$, $m_{\parallel}/m_0 = 0.021$, and $\Delta = 57 \text{ meV}$, corresponding to the C1 subband in a 50- \AA Hg_{0.75}Cd_{0.25}Te / 50- \AA Hg_{0.7}Cd_{0.3}Te SL.

The anisotropy in the resulting effective thermopower S_{eff} [Eq. (15)] and Lorentz number $L_{0,\text{eff}} = \kappa_{\text{eff}}/\sigma_{\text{eff}}T$ is shown in Fig. 6. For $\mu < 0$, S_{eff} along the growth and in-plane directions differ by $< 10\%$. This near isotropy is expected, since the carriers determining S_{eff} are near the zone center, where the effective-mass approximation is good. The anisotropy increases substantially as μ increases past 2Δ , reaching over 6000 at $\mu = 0.4 \text{ eV}$. From Fig. 6(b), the anisotropy in $L_{0,\text{eff}}$ is at most 30% and goes to zero in the large- μ limit, approaching the metallic value of $(\pi^2/3)(k_B/e)^2$. As ZT for this band structure is maximal for $\mu \sim 0$, the anisotropy in S_{eff} and $L_{0,\text{eff}}$ in the relevant parameter range are small.

These numerical results are also consistent with the idea that the induced fields are detrimental to ZT , as discussed in Appendix A. As shown by the dotted lines in Fig. 6(a), the induced fields present along low-symmetry directions reduce S_{eff} below S_{xx} . However, S_{eff} is always bounded by $S_{\text{eff}} = S_{xx}$ along the principal directions. Thus, optimal thermoelectric performance is achieved for samples cut along the principal axes.

VI. SUMMARY

This paper developed the transport theory relevant for anisotropic, multi-valleyed materials, taking into account the full tensorial structure of the electronic transport coefficients and including the effects of sample boundaries. Induced transverse fields are associated with samples cut along directions in which the conductivity had off-diagonal elements. These fields can be larger than the applied fields. Within the effective-mass and relaxation-time approximations and the neglect of intervalley scattering, the tensor characterizing the structure appears as a simple multiplicative factor of each of the transport coefficients. This factorization results in an isotropic thermopower and Lorentz number even in the presence of anisotropy. In a hypothetical material having no lattice thermal conductivity ZT would therefore be isotropic. For non-vanishing and sufficiently isotropic lattice thermal conductivity ZT is maximal for samples cut along the high-conductivity directions. Widely ranging numerical results suggest that the maximal ZT generally occurs along the principal direction which maximizes the ratio of the electronic to lattice thermal conductivity. An upper bound for ZT is given which generalizes the result of Mahan and Sofo¹¹ to anisotropic systems.

Application of these formal results to some systems of interest showed the following. (1) Bulk n-type Bi_2Te_3 exhibits induced transverse fields, reduced effective conductivity, and anisotropic ZT s. These effects should be easily observable. (2) In $\text{HgTe}/\text{Hg}_{1-x}\text{Cd}_x\text{Te}$ SLs, whose anisotropy is adjustable by varying the layer widths and composition, increased anisotropy is associated with larger induced fields. (3) The confining potential in *isolated* Bi_2Te_3 quantum wells splits the valley degeneracy and changes the masses from their bulk values. The latter features suggest that optimal ZT s are associated with wells grown along the trigonal direction. (4) The effect of non-parabolic dispersion on the thermopower is very small for the doping range over which ZT is maximal. The maximal thermopower occurs along principal directions, which supports the suggestion given in the previous paragraph.

ACKNOWLEDGMENTS

Discussions with E. Runge are gratefully acknowledged. This work was supported by DARPA through ONR Contract No. N00014-96-1-0887 and the NSF through Che9610501.

APPENDIX A:

In this appendix we present a unified form of the linear-response theory which, because of its explicit use of the Onsager coefficients, has the advantage of treating the electric and heat currents more symmetrically than in Sec. II. Note that, since the Onsager coefficients are assumed to be symmetric matrices, this formalism does not apply to monoclinic, triclinic, or chiral materials. The generalized fluxes \mathbf{J} are given in terms of the generalized forces \mathbf{f} by

$$\mathbf{J} = \underline{L}\mathbf{f} \quad (\text{A1})$$

with

$$\mathbf{J} = \left(J_x^e \ J_x^Q \ J_y^e \ J_y^Q \ J_z^e \ J_z^Q \right)^T = \begin{pmatrix} \mathbf{J}_{\parallel} \\ \mathbf{J}_{\perp} \end{pmatrix} \quad (\text{A2})$$

and

$$\mathbf{f} = \left(e\mathcal{E}_x \ -\nabla_x T/T \ e\mathcal{E}_y \ -\nabla_y T/T \ e\mathcal{E}_z \ -\nabla_z T/T \right)^T = \begin{pmatrix} \mathbf{f}_{\parallel} \\ \mathbf{f}_{\perp} \end{pmatrix} \quad (\text{A3})$$

where \mathbf{J}_{\parallel} and \mathbf{f}_{\parallel} contain the first two components and \mathbf{J}_{\perp} and \mathbf{f}_{\perp} the remaining four components of \mathbf{J} and \mathbf{f} , respectively. With respect to these conventions the matrix of Onsager coefficients, \underline{L} , assumes the form

$$\underline{L} = \begin{pmatrix} \underline{L}_{\parallel} & \underline{L}_{od}^T \\ \underline{L}_{od} & \underline{L}_{\perp} \end{pmatrix} \quad (\text{A4})$$

with

$$\underline{L}_{\parallel} = \begin{pmatrix} L_{xx}^{11} & L_{xx}^{21} \\ L_{xx}^{12} & L_{xx}^{22} \end{pmatrix}, \quad (\text{A5})$$

$$\underline{L}_{od} = \begin{pmatrix} L_{xy}^{11} & L_{xy}^{21} & L_{xz}^{11} & L_{xz}^{21} \\ L_{xy}^{12} & L_{xy}^{22} & L_{xz}^{12} & L_{xz}^{22} \end{pmatrix}^T \quad (\text{A6})$$

and

$$\underline{L}_{\perp} = \begin{pmatrix} L_{yy}^{11} & L_{yy}^{21} & L_{yz}^{11} & L_{yz}^{21} \\ L_{yy}^{12} & L_{yy}^{22} & L_{yz}^{12} & L_{yz}^{22} \\ L_{zy}^{11} & L_{zy}^{21} & L_{zz}^{11} & L_{zz}^{21} \\ L_{zy}^{12} & L_{zy}^{22} & L_{zz}^{12} & L_{zz}^{22} \end{pmatrix}. \quad (\text{A7})$$

Equation (A1) and the condition that $\mathbf{J}_{\perp} = 0$ yield

$$\mathbf{f}_{\perp} = -\underline{L}_{\perp}^{-1} \underline{L}_{od} \mathbf{f}_{\parallel}; \quad (\text{A8})$$

hence,

$$\mathbf{J}_{\parallel} = \underline{L}_{\text{eff}} \mathbf{f}_{\parallel} \quad (\text{A9})$$

with

$$\underline{L}_{\text{eff}} = \underline{L}_{\parallel} - \underline{L}_{od}^T \underline{L}_{\perp}^{-1} \underline{L}_{od} \equiv \underline{L}_{\parallel} - \underline{N}_{\parallel} \quad (\text{A10})$$

It can be shown that $\underline{N}_{\parallel} > 0$ and $\underline{L}_{\text{eff}} \geq 0$. We may decompose \mathbf{J}_{\parallel} into external and induced parts as follows:

$$\mathbf{J}_{\parallel} = \mathbf{J}^{\text{ext}} + \mathbf{J}^{\text{ind}} \quad (\text{A11})$$

with

$$\mathbf{J}^{\text{ext}} = \underline{L}_{\parallel} \mathbf{f}_{\parallel} \quad (\text{A12})$$

and

$$\mathbf{J}^{\text{ind}} = -\underline{N}_{\parallel} \mathbf{f}_{\parallel}. \quad (\text{A13})$$

In Sec. II it was found that, for an applied electric field only ($\mathbf{f}_{\parallel} = (e\mathcal{E}_x, 0)$), the induced electric current opposes the external electric current because $\sigma_{\text{eff}} \leq \sigma_{\parallel}$, and likewise for an applied thermal gradient only, the induced heat current opposes the external heat current. Physical intuition suggests that these results should generalize to the case where both an applied electric field and applied thermal gradient are present. Then we expect that, if both components of \mathbf{f} have the same sign, \mathbf{J}^{ind} should oppose \mathbf{J}^{ext} in the sense that they lie in opposite quadrants of the plane spanned by J_x^e and J_x^Q . Although we have not proven this conjecture, it is consistent with numerical results for randomly constructed matrices of Onsager coefficients. Undoubtedly a proof requires a general microscopic model. Finally, we note that the entropy generation is given by

$$-T \left. \frac{\partial S}{\partial t} \right|_{\text{field}} = \mathbf{J} \cdot \mathbf{f} = \mathbf{J}^{\text{ext}} \cdot \mathbf{f}_{\parallel} + \mathbf{J}^{\text{ind}} \cdot \mathbf{f}_{\parallel}. \quad (\text{A14})$$

Since $\underline{L}_{\parallel} > 0$ and $\underline{N}_{\parallel} > 0$, we have $\mathbf{J}^{\text{ext}} \cdot \mathbf{f}_{\parallel} > 0$ and $\mathbf{J}^{\text{ind}} \cdot \mathbf{f}_{\parallel} < 0$. Thus, external currents *decrease* $\dot{S}|_{\text{field}}$ but induced currents *increase* $\dot{S}|_{\text{field}}$.

APPENDIX B:

We present here a derivation of an upper bound of the Sofo and Mahan form¹¹ for an anisotropic material. From $\underline{\sigma} = \underline{A}\sigma_0$ we infer

$$\sigma_{\text{eff}} = \sigma_0 a_0 \quad (\text{B1})$$

with

$$a_0 = A_{xx} - A_{xy} \frac{A_{yx}A_{zz} - A_{yz}A_{zx}}{A_{yy}A_{zz} - A_{yz}A_{zy}} - A_{xz} \frac{A_{zx}A_{yy} - A_{zy}A_{yx}}{A_{zz}A_{yy} - A_{yz}A_{zy}}. \quad (\text{B2})$$

When the κ_ℓ -dependence in Eq. (59) is taken into account, we find similarly

$$\kappa_e^* = \kappa_e a(\kappa_\ell) \quad (\text{B3})$$

with $a(\kappa_\ell = 0) = a_0$ and

$$a(\kappa_\ell) = A_{xx} - A_{xy} \frac{A_{yx}(A_{zz} + \kappa_\ell/\kappa_e) - A_{yz}A_{zx}}{(A_{yy} + \kappa_\ell/\kappa_e)(A_{zz} + \kappa_\ell/\kappa_e) - A_{yz}A_{zy}} - A_{xz} \frac{A_{zx}(A_{yy} + \kappa_\ell/\kappa_e) - A_{zy}A_{yx}}{(A_{yy} + \kappa_\ell/\kappa_e)(A_{zz} + \kappa_\ell/\kappa_e) - A_{yz}A_{zy}}. \quad (\text{B4})$$

Therefore

$$ZT = \frac{T\sigma_0 S_0^2 a_0}{(\kappa_0 - T\sigma_0 S_0^2) a(\kappa_\ell) + \kappa_\ell}. \quad (\text{B5})$$

Following Mahan and Sofo, introduce dimensionless integrals

$$I_n = \int_{-\mu/k_B T}^{\infty} dx \frac{e^x}{(e^x + 1)^2} s(x) x^n, \quad s(x) = \hbar r_0 \mathcal{T}(\mu + xkT), \quad (\text{B6})$$

where r_0 is the Bohr radius. In terms of these moments,

$$\sigma_0 = \tilde{\sigma}_0 I_0 \quad (\text{B7})$$

$$\sigma_0 S_0 = (k_B/e) \tilde{\sigma}_0 I_1 \quad (\text{B7})$$

$$\kappa_0 = (k_B/e)^2 T \tilde{\sigma}_0 I_2 \quad (\text{B8})$$

where $\tilde{\sigma}_0 = e^2/\hbar r_0$ has dimensions of conductivity. Then

$$ZT = \frac{T(k_B/e)^2 \tilde{\sigma}_0^2 I_1^2 / \tilde{\sigma}_0 I_0}{((k_B/e)^2 T \tilde{\sigma}_0 I_2 - T(k_B/e)^2 \tilde{\sigma}_0 I_1^2 / I_0) a(\kappa_\ell) / a_0 + \kappa_\ell / a_0} \quad (\text{B9})$$

$$= \frac{\tilde{\alpha} I_1^2 / I_0}{(\tilde{\alpha} I_2 - \tilde{\alpha} I_1^2 / I_0) a(\kappa_\ell) / a_0 + 1 / a_0} \quad (\text{B10})$$

$$= \frac{\xi}{(1 - \xi) a(\kappa_\ell) / a_0 + B} \quad (\text{B11})$$

with $\tilde{\alpha} = (k_B/e)^2 T \tilde{\sigma}_0 / \kappa_\ell$,

$$\xi = I_1^2 / I_0 I_2, \quad (\text{B12})$$

and $B = 1/\tilde{\alpha} I_2 a_0 = \kappa_\ell / \kappa_0 a_0$. By the Cauchy-Schwarz inequality, $0 \leq \xi \leq 1$. The limit as ξ tends to 1 maximizes the figure of merit by maximizing the numerator and minimizing the denominator in Eq. (B11). From Eq. (B4) it may be seen that for $\kappa_\ell / \kappa_e = \kappa_\ell / (k_B/e)^2 T \tilde{\sigma}_0 I_2 (1 - \xi)$ sufficiently large, $a(\kappa_\ell)$ tends to A_{xx} , and certainly this condition is met as $1 - \xi$ tends to zero. Thus as $\xi \rightarrow 1$ we have that

$$ZT \rightarrow \frac{\xi}{(1 - \xi) A_{xx} / a_0 + B} \leq \frac{1}{B} = \frac{\kappa_0 a_0}{\kappa_\ell}. \quad (\text{B13})$$

- ¹ L. D. Hicks and M. S. Dresselhaus, Phys. Rev. B **47**, 12727 (1993).
- ² G. D. Mahan and H. B. Lyon, Jr., J. Appl. Phys. **76**, 1899 (1994).
- ³ J. O. Sofo and G. D. Mahan, Appl. Phys. Lett. **65**, 2690 (1994).
- ⁴ D. A. Broido and T. L. Reinecke, Phys. Rev. B **51**, 13797 (1995).
- ⁵ L. D. Hicks, T. C. Harman, X. Sun, and M. S. Dresselhaus, Phys. Rev. B **53**, R10493 (1996).
- ⁶ D. A. Broido and T. L. Reinecke, Appl. Phys. Lett. **70**, 2834 (1997) and unpublished.
- ⁷ L. D. Hicks, T. C. Harman, and M. S. Dresselhaus, Appl. Phys. Lett. **63**, 3230 (1993).
- ⁸ D. A. Broido and T. L. Reinecke, Appl. Phys. Lett. **67**, 1170 (1995).
- ⁹ L. D. Hicks and M. S. Dresselhaus, Phys. Rev. B **47**, 16631 (1993).
- ¹⁰ D. A. Broido and T. L. Reinecke, Appl. Phys. Lett. **67**, 100 (1995).
- ¹¹ G. D. Mahan and J. O. Sofo, Proc. Natl. Acad. Sci. USA **93**, 7436 (1996).
- ¹² *Semiconductors: Other than Group IV Elements and III-V Compounds*, edited by O. Madelung (Springer, New York, 1992).
- ¹³ H. J. Goldsmid, *Thermoelectric Refrigeration* (Plenum, New York, 1964).
- ¹⁴ N. F. Johnson, H. Ehrenreich, P. M. Hui, and P. M. Young, Phys. Rev. B **41**, 3655 (1990); M. E. Flatté, C. H. Grein, H. Ehrenreich, R. H. Miles, and H. Cruz, J. Appl. Phys. **78**, 4552 (1995) and references therein.
- ¹⁵ G. Bastard, in *Proceedings of the NATO Advanced Study Institute on Molecular Beam Epitaxy in Heterostructures, Erice, July, 1983*, edited by L. L. Chang and K. Ploog (Martinus-Nijhoff, Dordrecht, 1984), p. 381.
- ¹⁶ Actual quantum wells are embedded in another solid whose finite thermal conductivity acts as a parasitic effect that lowers ZT . Initially optimistic ZT estimates in these systems¹ have been revised downward after including this effect.^{2,3}
- ¹⁷ L. Esaki and R. Tsu, IBM J. Res. Dev. **14**, 61 (1970).
- ¹⁸ J. C. Brice, in *Properties of Mercury Cadmium Telluride*, edited by J. Brice and P. Capper, EMIS Datareview Series No. 3 (INSPEC, New York, 1987), Ch. 5.1.
- ¹⁹ N. F. Johnson, P. M. Hui, and H. Ehrenreich, Phys. Rev. Lett. **61**, 1993 (1988); P. M. Hui, N. F. Johnson, and H. Ehrenreich, J. Vac. Sci. Technol. A **7**, 424 (1989).
- ²⁰ R. Dornhaus and D. Nimtz, in *Narrow-Gap Semiconductors*, edited by G. Höhler (Springer, New York, 1983).
- ²¹ E. O. Kane, in *Narrow Gap Semiconductors: Physics and Applications*, edited by W. Zawadzki, Lecture Notes in Physics Vol. 133 (Springer, New York, 1981), p. 19.
- ²² J. N. Schulman and Y.-C. Chang, Phys. Rev. B **33**, 2594 (1986).
- ²³ R. Granger and C. M. Pelletier, J. Crys. Growth **138**, 486 (1994).
- ²⁴ J. C. Brice, in Ref. 18, Ch. 1.9.

TABLE I. Room temperature energy gap E_g , spin-orbit splitting Δ , and heavy-hole effective mass m_{HH} for a HgTe/Hg_{0.15}Cd_{0.85}Te superlattice. The valence band offset is 0.30 eV from a linear interpolation of the value in Ref. 19, and the momentum matrix element $\langle 2/m_0 \rangle < Z|p_z|S \rangle^2 = 18.0$ eV (Ref. 20).

	HgTe	Hg _{0.15} Cd _{0.85} Te
E_g at 300 K (eV) ^a	-0.166	1.191
Δ (eV) ^b	1.0	0.9
m_{HH}/m_0^c	0.7	0.7

^aRef. 18.

^bRef. 21.

^cRef. 22.

TABLE II. Parameters and thermoelectric performance in HgCd/HgCdTe superlattices (SLs). m_{\perp} and m_{\parallel} are the $C1$ effective masses along and normal to the growth axis, $(\mathcal{E}^{\text{ind}}/F^{\text{ext}})_{\text{max}}$ is the maximal relative magnitude of the induced field, ϕ_{max} is the angle relative to the SL planes at which the sample must be cut to obtain this field, $(ZT)_{\text{max}}$ is the maximal figure of merit for the SL, and $(ZT)_{\text{alloy}}$ is that for the equivalent alloy.

	SL (1) 30-Å HgTe / 20-Å Hg _{0.15} Cd _{0.85} Te	SL (2) 20-Å HgTe / 40-Å Hg _{0.15} Cd _{0.85} Te
Band structure: ^a		
E_g (eV)	0.25	0.46
m_{\perp}/m_0	0.038	0.110
m_{\parallel}/m_0	0.025	0.043
m_{\parallel}/m_{\perp}	0.66	0.39
Transport parameters:		
τ (s) ^b	5.3×10^{-14}	2.6×10^{-14}
κ_{ℓ} (mW / cm K) ^c	8.2	12
Thermoelectric performance: ^d		
$(\mathcal{E}^{\text{ind}}/F^{\text{ext}})_{\text{max}}$	0.21	0.48
ϕ_{max} (rad)	0.22 π	0.18 π
$(ZT)_{\text{max}}$	0.14	0.086
$(ZT)_{\text{alloy}}$	0.12	0.061

^aBased on the parameters in Tab. I.

^bFrom the mobility data presented in Ref. 23.

^cQuadratic fit to the data in Ref. 24.

^dThis work.

FIG. 1. Constant-energy surfaces of the conduction band valleys in Bi_2Te_3 . The bisectrix, binary, and trigonal directions are indicated.

FIG. 2. Effect of induced transverse fields in bulk n-type Bi_2Te_3 . (a) Normalized induced field F_z/F_x [Eq. (4)] and (b) microscopic (σ_{xx} , dot-dashed line) and effective (σ_{eff} , solid line) conductivities [Eq. (18)] for the sample geometry shown in the inset.

FIG. 3. ZT of n-type Bi_2Te_3 at 300 K for (a) a hypothetical material with $\kappa_\ell = 0$ and (b) $\kappa_\ell = 1.5 \text{ W / m K}$, the bulk in-plane value, as a function of the direction in which the sample is cut (defined in the inset).

FIG. 4. Relative magnitude of the induced electric field $\mathcal{E}^{\text{ind}}/F^{\text{ext}}$ in a superlattice as a function of the angle ϕ defined in the inset for several values of the conductivity ratio $\sigma_{\text{min}}/\sigma_{\text{max}}$ [Eq. (66)].

FIG. 5. Maximal ZT at 300 K for an isolated Bi_2Te_3 quantum well within the multi-ellipsoid model of Sec. IV C as a function of well width for wells grown along the trigonal (heavy dot-dashed line) or binary (heavy solid line) directions. Results for the equivalent-ellipsoid model of Ref. 1 for wells grown along the trigonal (thin dot-dashed line) and binary (thin solid line) directions are also shown.

FIG. 6. (a) Effective thermopower S_{eff} and (b) effective Lorentz number $L_{0,\text{eff}} = \kappa_{\text{eff}}/\sigma_{\text{eff}}T$ as a function of chemical potential for the superlattice described in Sec. V. Shown are samples cut along $\phi = 0$ (heavy solid line), $\pi/4$ (heavy dotted line), and $\pi/2$ (heavy dashed line) as defined in the inset to Fig. 4. The results for $\phi = \pi/4$ neglecting the effects of the induced fields are also presented (light dotted line). The metallic limit of $L_0/(k_B/e)^2 = \pi^2/3$ is indicated in (b).

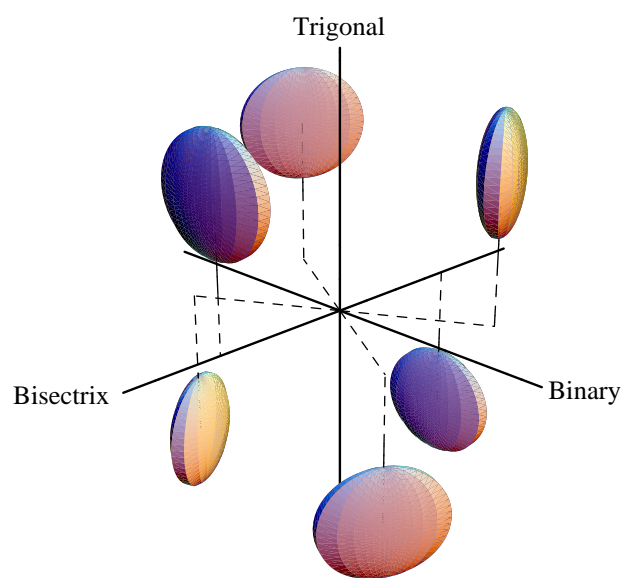


Fig. 1, Bies *et al.*, Phys. Rev. B

Bulk Bi_2Te_3

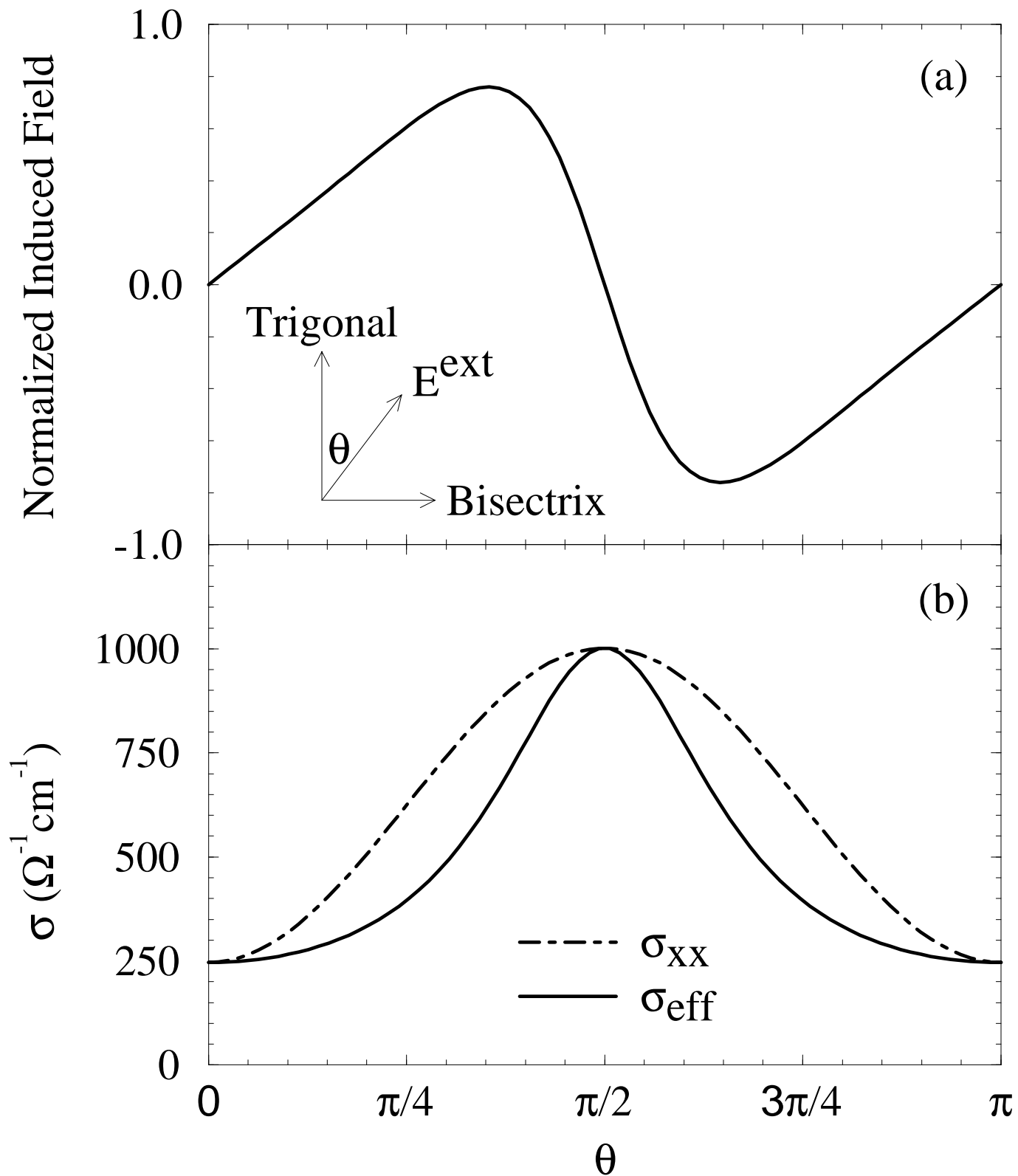
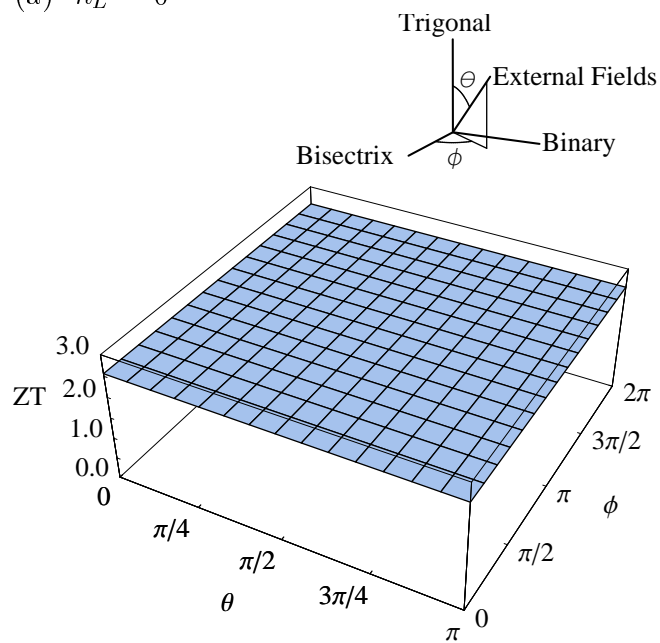


Fig. 2, Bies *et al.*, Phys. Rev. B

(a) $\kappa_L = 0$



(b) $\kappa_L = 1.5 \text{ W / m K}$

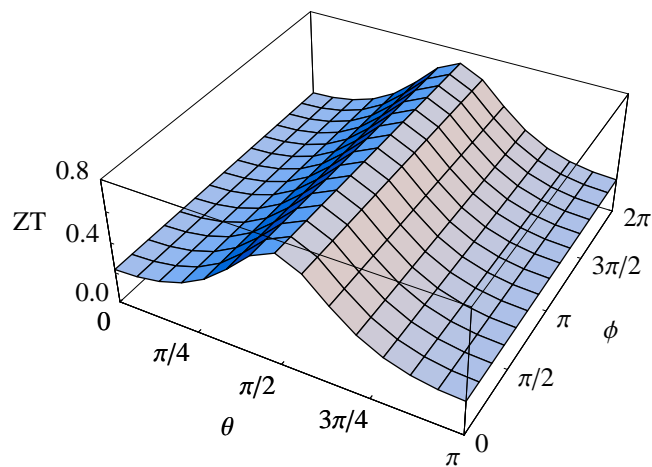


Fig. 3, Bies *et al.*, Phys. Rev. B

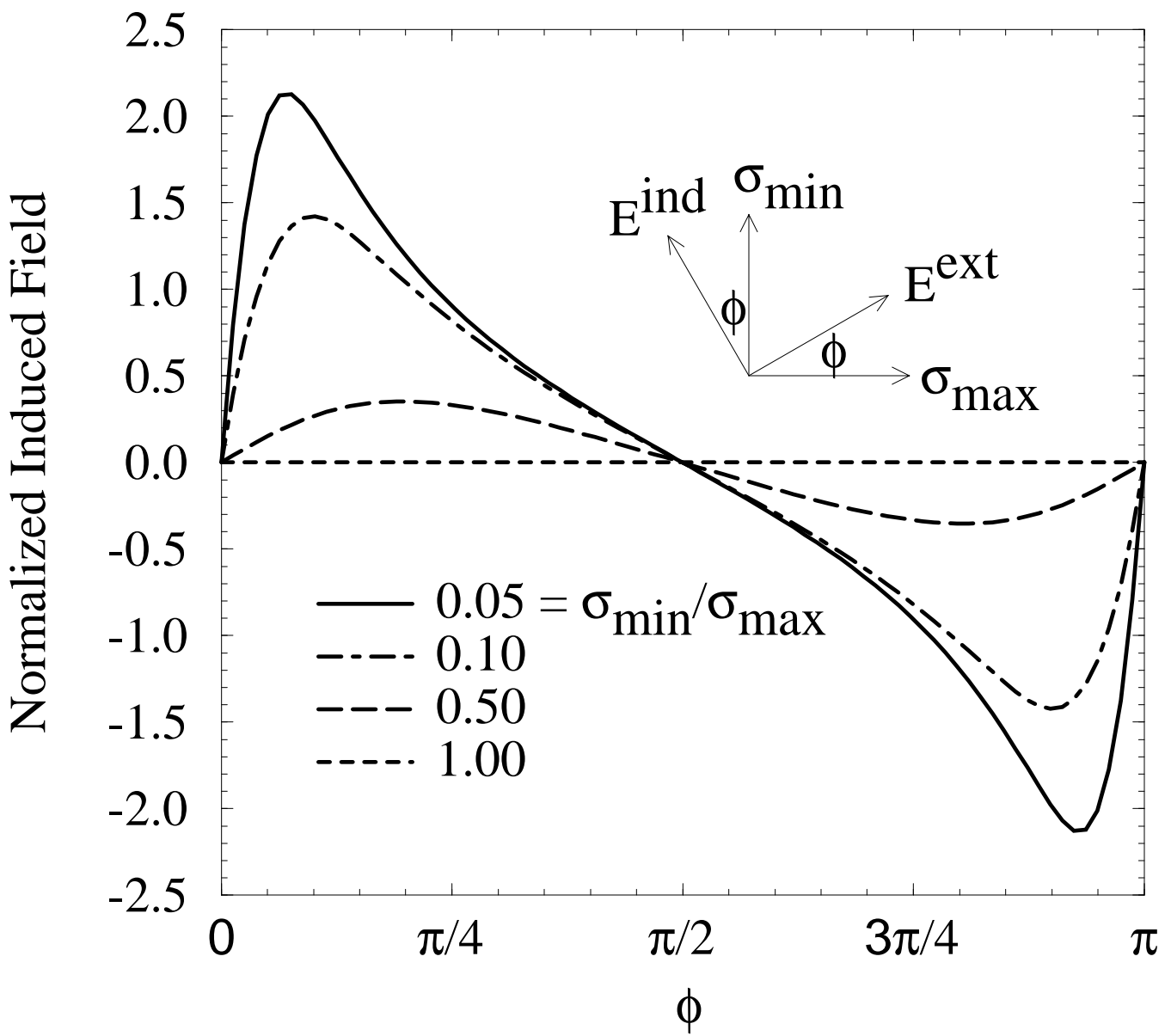


Fig. 4, Bies *et al.*, Phys. Rev. B

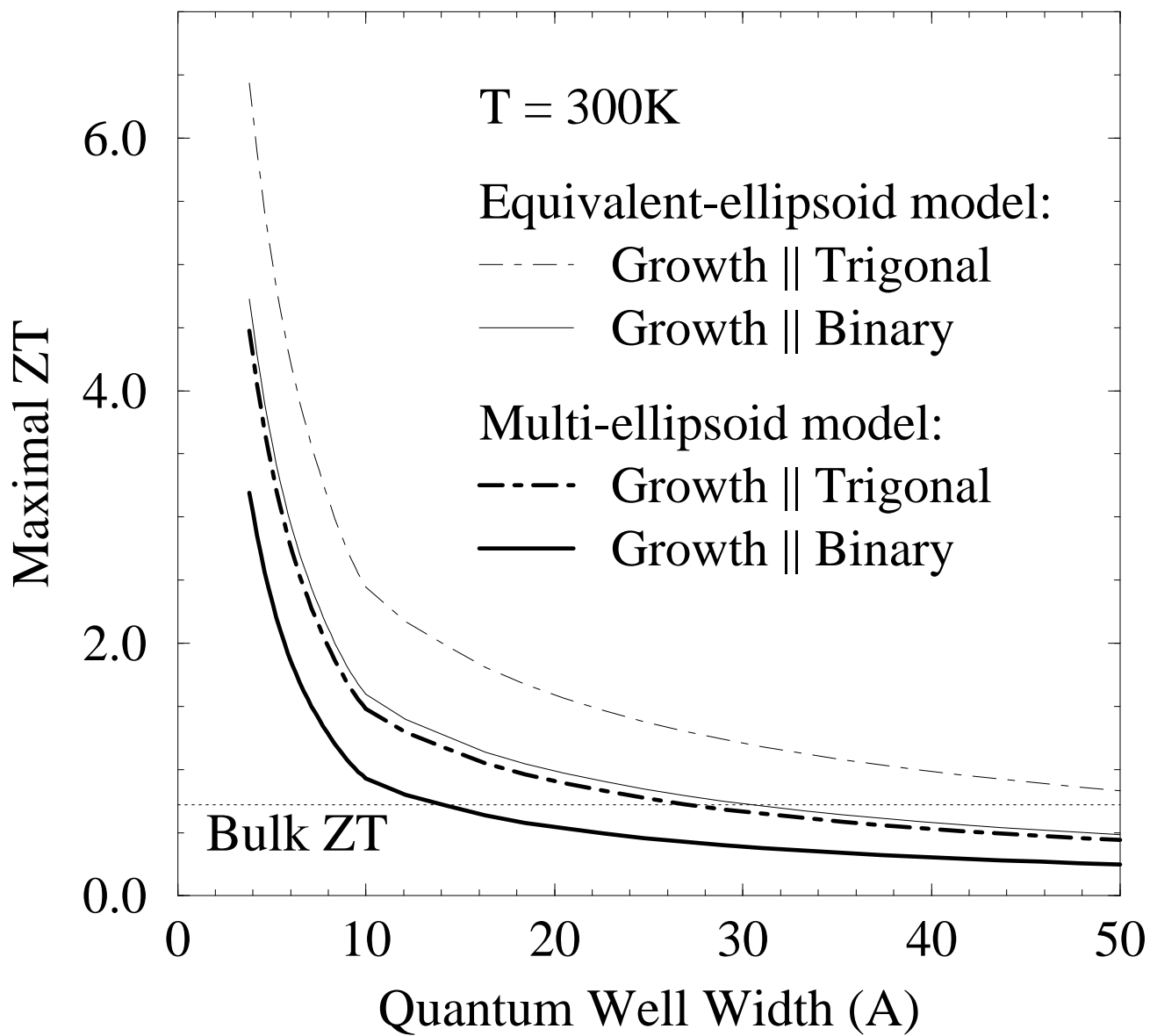


Fig. 5, Bies *et al.*, Phys. Rev. B

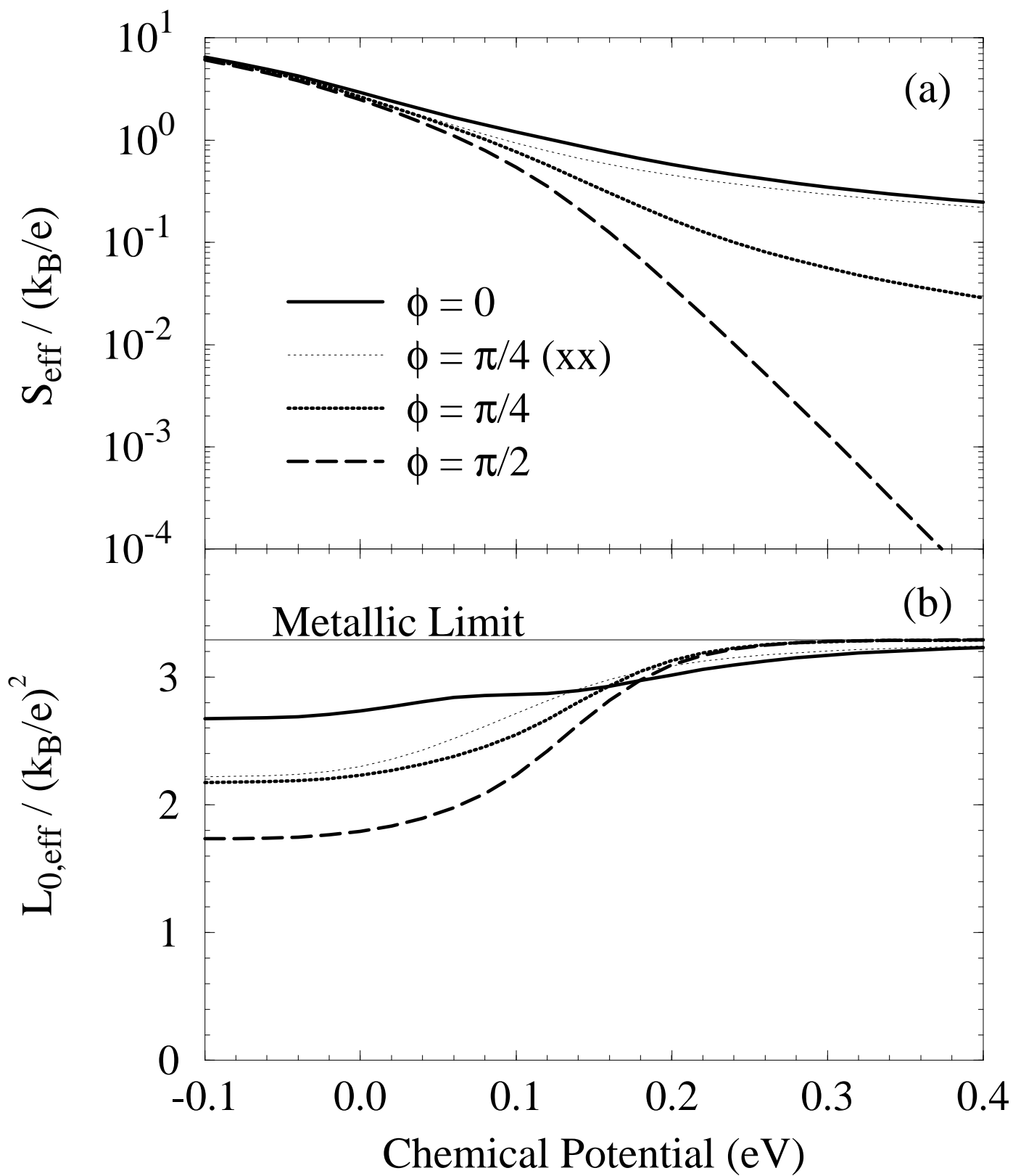


Fig. 6, Bies *et al.*, Phys. Rev. B